J. Fluid Mech. (2013), *vol.* 733, *pp.* 171–188.
doi:10.1017/jfm.2013.407

Particle capture by a circular cylinder in the vortex-shedding regime

Alexis Espinosa-Gayosso[1,2],†, Marco Ghisalberti[1], Gregory N. Ivey[1,2] and Nicole L. Jones[1,2]

[1]School of Environmental Systems Engineering, University of Western Australia, Crawley, WA 6009, Australia

[2]UWA Oceans Institute, University of Western Australia, Crawley, WA 6009, Australia

(Received 7 January 2013; revised 26 June 2013; accepted 5 August 2013; first published online 19 September 2013)

Particle capture, whereby suspended particles contact and adhere to a solid surface (a 'collector'), is an important mechanism for a range of environmental processes including suspension feeding by corals and 'filtering' by aquatic vegetation. In this paper, we use two- and three-dimensional direct numerical simulations to quantify the capture efficiency (η) of low-inertia particles by a circular cylindrical collector at intermediate Reynolds numbers in the vortex-shedding regime (i.e. for $47 < Re \leqslant 1000$, where Re is the collector Reynolds number). We demonstrate that vortex shedding induces oscillations near the leading face of the collector which greatly affect the quantity and distribution of captured particles. Unlike in steady, low-Re flow, particles directly upstream of the collector are not the most likely to be captured. Our results demonstrate the dependence of the time-averaged capture efficiency on Re and particle size, improving the predictive capability for the capture of particles by aquatic collectors. The transition to theoretical high-Reynolds-number behaviour (i.e. $\eta \sim Re^{1/2}$) is complex due to comparatively rapid changes in wake conditions in this Reynolds number range.

Key words: biological fluid dynamics, boundary layer structure, particle/fluid flows

1. Introduction

'Particle capture' is a process by which particles in suspension contact a solid structure ('collector') and adhere to its surface. Many environmental processes in aquatic systems are controlled by particle-capture mechanisms: suspension feeding (Wildish & Kristmanson 1997), seagrass pollination (Ackerman 2006), larval settlement (Harvey, Bourget & Ingram 1995) and 'filtering' by aquatic vegetation (Palmer *et al.* 2004), among others. Despite its ecological importance, the phenomenon of particle capture, particularly in the vortex-shedding regime, remains poorly understood.

In particle-capture research, collectors are usually simplified as cylindrical structures (representing the capturing filaments of suspension feeders or vegetation stems) and particles as spheres. The capture efficiency (η) of a cylindrical collector can be defined as the ratio of the number of particles captured (N_c) to the number of particles whose centres would have passed through the space occupied by the collector were it not

† Email address for correspondence: Alexis.Espinosa-Gayosso@uwa.edu.au

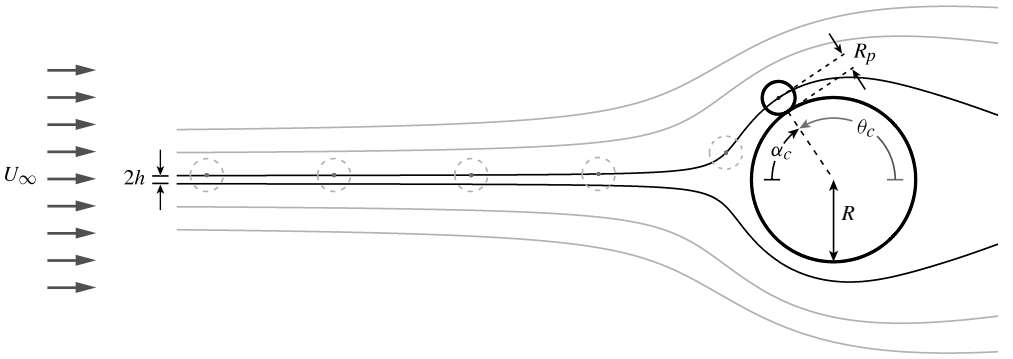

FIGURE 1. Steady flow conceptualization of particle capture by direct interception. Particle pathlines coincide with the flow streamlines. The maximum angle of capture (α_c or θ_c, depending on the coordinate system used) is indicated by the dotted line within the collector. The limiting particle trajectory, which is the pathline of a particle captured at the maximum angle of capture, is shown. The separation between limiting particle trajectories upstream of the influence of the cylindrical collector ($2h$) is the 'upstream window of capture' and is used to define the efficiency of capture by direct interception, η_{DI} (1.7).

present in the flow (N_a):

$$\eta = \frac{N_c}{N_a}. \tag{1.1}$$

Here we consider perfect particle–collector adhesion, such that all particles are assumed to be captured when they contact the cylinder surface.

As discussed by Espinosa-Gayosso *et al.* (2012), direct interception (where particle centres follow the fluid exactly and contact with the collector occurs due to the finite particle size) has been recognized as an important capture mechanism in aquatic systems (figure 1 displays the steady flow conceptualization of particle capture by direct interception). When compared with direct interception, inertial and diffusive effects on particle capture are typically neglected in the aquatic systems of interest, due to the low Stokes numbers (St) and high Péclet numbers (Pe) of suspended particles, respectively (Espinosa-Gayosso *et al.* 2012). These two parameters are defined as

$$St = \frac{\rho_p D_p^2 U_\infty}{9\mu D} \tag{1.2}$$

and

$$Pe = \frac{U_\infty D}{\Gamma_p}, \tag{1.3}$$

where D_p is the particle diameter, D is the collector diameter, ρ_p is the particle density, U_∞ is the uniform upstream fluid velocity, μ is the fluid viscosity and Γ_p is the particle diffusivity. Capture efficiency by direct interception depends on two different parameters (Espinosa-Gayosso *et al.* 2012):

$$\eta_{DI} = \eta_{DI}(r_p, Re), \tag{1.4}$$

where r_p is the particle size ratio and Re is the Reynolds number of the collector. The definition of these two parameters is

$$r_p = \frac{D_p}{D} \equiv \frac{R_p}{R} \tag{1.5}$$

and

$$Re = \frac{\rho U_\infty D}{\mu}, \tag{1.6}$$

where R_p is the particle radius, R is the collector radius, ρ is the fluid density and μ is the fluid viscosity.

Here we investigate direct interception of low-inertia particles by circular cylindrical collectors. It is assumed that the particles follow the fluid exactly and have a negligible influence on the flow field. The authors recently obtained an expression for estimating the capture efficiency of low-inertia particles by cylindrical collectors over the range of Re prior to the onset of vortex shedding (i.e. $Re \leqslant 47$) and a range of particle size ratios relevant to aquatic systems ($r_p \leqslant 1.5$) (Espinosa-Gayosso *et al.* 2012). In the steady flow conceptualization of particle capture (figure 1), pathlines for low-inertia particles coincide with the streamlines and the capture efficiency by direct interception can thus be defined as

$$\eta_{DI} = \frac{2h}{D} \equiv \frac{h}{R}. \tag{1.7}$$

However, when vortex shedding is present in the wake, it induces pressure and velocity oscillations near the leading face of the collector invalidating the steady flow conceptualization of particle capture. Self-induced upstream oscillations have been observed in two-dimensional numerical studies (Jordan & Fromm 1972; Braza, Chassaing & Minh 1986) and in experiments (Dwyer & McCroskey 1973; Paxson & Mayle 1990), although the strength and the extent of these oscillations have not been clearly described. In this study we describe, for the first time, the spatial variability of the self-induced oscillatory conditions near the leading face of the collector and their influence on particle trajectories and capture efficiency.

The transition from the steady two-dimensional flow regime to the unsteady two-dimensional vortex-shedding regime at $Re_1 \simeq 47$ is not the only change in flow past a circular cylinder that is relevant here. The next transition occurs at $Re_2 \simeq 180$, when three-dimensional vortex shedding appears; a second type of three-dimensional vortex shedding starts at $Re_3 \simeq 260$ (Williamson 1988; Henderson 1997). Another transition occurs at $Re_4 \simeq 1000$ due to the instability of the separating shear layers from the side of the cylinder (Bloor 1964; Norberg 1994), with many others appearing at higher Re (Williamson 1996; Zdravkovich 1997). Such transitions induce significant changes in skin friction, wake pressure and the frequency of wake oscillation (Henderson 1995; Williamson 1996), likely resulting in changes in capture efficiency.

Previous numerical (Haugen & Kragset 2010) and experimental (Palmer *et al.* 2004) studies have suggested that, when $Re > 47$, the time-averaged capture efficiency of small particles on circular cylinder collectors may be described by an expression of the form $\overline{\eta_{DI}} \approx k_1 Re^{0.7} {r_p}^2$, where k_1 is a constant of proportionality. While simple, this expression has three main disadvantages: (i) it fails to describe the changes induced by the flow transitions mentioned above; (ii) it fails to describe the tendency towards the $\eta \sim Re^{1/2}$ proportionality predicted by boundary-layer theory for high Re (Parnas & Friedlander 1984; Haugen & Kragset 2010); and (iii) it is restricted to particles of vanishing size ratio ($r_p \to 0$) (Friedlander 2000) while, in reality, aquatic collectors can

capture particles with $r_p \sim O(1)$ (Harvey *et al.* 1995; Shimeta & Koehl 1997). Here we aim to provide a physically-based description of capture efficiency that is free of such limitations.

In the present paper, we have used two- and three-dimensional direct numerical simulations (DNS) of flow past a circular cylinder to quantify particle capture by direct interception. Reynolds number and particle size ratio ranges relevant to aquatic systems are considered ($47 \leqslant Re \leqslant 1000$ and $0 < r_p \leqslant 0.5$). As part of this analysis, we investigate the time-averaged and oscillatory components of the flow upstream of the collector and the influence of these oscillations on particle trajectories and capture efficiency.

2. Basic equations of fluid motion and numerical methods

2.1. *Equations of motion*

The governing equations are the continuity and Navier–Stokes equations for unsteady and incompressible flow. Here they are non-dimensionalized with the uniform free-stream velocity U_∞ as the velocity scale, and the radius of the collector R as the length scale:

$$\nabla \cdot \boldsymbol{u} = 0 \tag{2.1}$$

and

$$\frac{\partial \boldsymbol{u}}{\partial t} + (\nabla \boldsymbol{u})\boldsymbol{u} = -\nabla p + \frac{2}{Re}\nabla^2 \boldsymbol{u}, \tag{2.2}$$

where $\boldsymbol{u}$ is the non-dimensional velocity vector, p is the non-dimensional pressure, t is the non-dimensional time and Re is the Reynolds number based on the diameter of the collector, as defined by (1.6).

Most of our results are presented in a non-dimensional cylindrical coordinate system (r, θ, z) with the z-axis coincident with the axis of the collector and θ measured anticlockwise. We also make use of α, the angle measured from the leading edge in a clockwise manner, as indicated in figure 1. When relevant, some quantities are presented in a non-dimensional Cartesian coordinate system (x, y, z) with the origin and the z-axis coincident with the cylindrical system.

2.2. *Spatial discretization*

For the two-dimensional DNS, the flow was solved in the rectangular domain $-200 \leqslant x \leqslant 80$ and $-200 \leqslant y \leqslant 200$, which is wide enough to avoid blockage effects (Lange, Durst & Breuer 1998; Posdziech & Grundmann 2007). The mesh topology is the same as in Wu *et al.* (2004), where an H-type (rectangular) mesh is defined in most of the domain except adjacent to the cylinder where an O-type ring (cylindrical mesh) is used, with a transition region between the two mesh types. The O-type ring spanned from $r = 1$ (the collector surface) to $r = 1.2$. The tangential direction of this ring was discretized into 744 uniform cells and a non-uniform grid was used in the radial direction. The radial size of the cells adjacent to the collector surface was $\Delta r \approx 1.0 \times 10^{-3}$, less than the displacement thickness at the leading edge for all Re considered here (Bouhairie & Chu 2007). The O-type mesh merged smoothly into the H-type mesh, which started exactly at the square defined by the diagonal points $(-1.6, -1.6)$ and $(1.6, 1.6)$ in Cartesian coordinates. The H-type mesh covered the rest of the domain, with cell sizes gradually expanding from $\Delta x, y = 0.0065$ to a maximum of $\Delta x, y = 1.6$ close to the domain boundaries. A fine mesh size of at most $\Delta x, y_{wake} = 0.05$ was applied in the wake region.

For the three-dimensional DNS, the axial extent of the domain ($-9.6 \leqslant z \leqslant 9.6$) was greater than twice the size of the most unstable wavelength of mode-A three-dimensional vortex shedding (Henderson 1997; Posdziech & Grundmann 2001). The axial direction was discretized into 128 uniform cells close to the cylinder, with a gradual reduction to 8 cells in the far field. A refinement of at least 32 cells was applied in the wake region.

2.3. *Numerical methods and boundary conditions*

The open-source code OpenFOAM®[‡] was used to solve (2.1) and (2.2) with a finite volume method of second order in space (Ferziger & Peric 2002) together with a three-level backward scheme in time, which is also of second order (Ferziger & Peric 2002). The time step was small enough to keep the maximum Courant number below 0.20. The pressure–velocity coupling was solved with the PISO algorithm (Issa 1986) in which convergence was deemed to be satisfied when the initial residuals of the pressure and momentum equations fell below 1×10^{-6}.

The following velocity boundary conditions were applied: (i) no-slip no-flux boundary conditions at the cylinder surface; (ii) a fixed uniform free stream at the upstream boundary ($(u_x, u_y, u_z) = (1, 0, 0)$ at $x_{inlet} = -200$); (iii) a zero-gradient condition perpendicular to the downstream boundary at $x_{outlet} = 80$; (iv) no-flux free-slip conditions at the lateral boundaries ($y = \pm 200$); and (v) cyclic conditions at the axial boundaries ($z = \pm 9.6$) in the three-dimensional DNS. For the pressure, a zero-gradient condition was applied at all boundaries except the outlet, where a fixed value of $p_{outlet} = 0$ was set, and at the cyclic axial boundaries.

3. Flow conditions near the collector

3.1. *The agreement between the present DNS and experimental data*

As discussed in § 1, there are several regimes of flow past a circular cylinder for different Re. Regime transitions induce changes in parameters such as the base suction coefficient

$$-C_{pb} = -\frac{\overline{P_b} - P_\infty}{\rho U_\infty^2/2}, \tag{3.1}$$

the drag coefficient

$$C_D = \frac{\overline{F_D}}{\rho U_\infty^2 D/2}, \tag{3.2}$$

and the Strouhal number

$$Str = \frac{D}{U_\infty T} \tag{3.3}$$

(see Henderson 1995, 1997). Here, $\overline{P_b}$ is the time average of the pressure at the trailing edge of the cylinder and P_∞ is the pressure at the upstream boundary, $\overline{F_D}$ is the time-averaged drag force on the cylinder per unit length and T is the peak period of wake oscillation.

The base suction coefficient varies significantly between regimes (figure 2*a*). At low Re, the flow is steady and symmetric and the base suction decreases gradually with increasing Re. Above $Re_1 \simeq 47$, the flow becomes unstable and two-dimensional vortex

[‡] OpenFOAM® is a registered trade mark of OpenCFD Limited, the producer of OpenFOAM software.

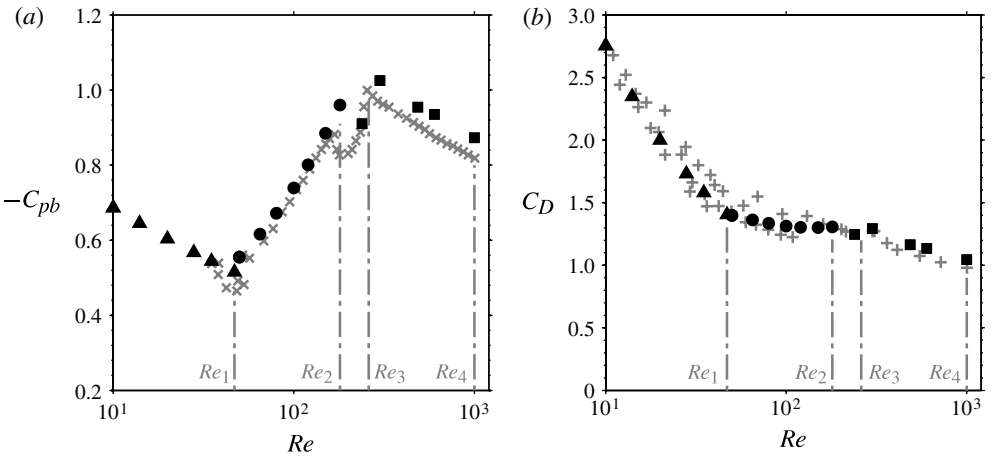

FIGURE 2. The agreement of the present DNS with existing experimental data for $Re \leqslant 1000$. (*a*) Base suction coefficient $-C_{pb}$. (*b*) Drag coefficient C_D. (▲) Two-dimensional steady flow DNS (Espinosa-Gayosso *et al.* 2012). (●) Present two-dimensional DNS. (■) Present three-dimensional DNS. (×) Experiments of Williamson & Roshko (1990). (+) Experiments of Wieselsberger (1921). (The vertical lines indicate the regime transitions as explained in §§ 1 and 3.1.)

shedding appears in the wake; the time-averaged pressure at the trailing edge drops and $-C_{pb}$ increases with Re. At $Re_2 \simeq 180$ and at $Re_3 \simeq 260$ two more changes can be observed as the flow transitions into distinct regimes of three-dimensional vortex shedding (Williamson & Roshko 1990; Henderson 1997). As seen in figure 2(*a*), our DNS estimates of the base suction coefficient are in good agreement with existing experimental data for $Re \leqslant 1000$. Our numerical estimates of the drag coefficient C_D (figure 2*b*) and the Strouhal number St (not shown) are also in excellent agreement with experiment. The relationships between these parameters and Re change dramatically at the transition points (Henderson 1997). In § 4.3, we show that capture efficiency exhibits similar behaviour.

3.2. *Oscillatory conditions near the leading face of the collector*

A series of instantaneous tangential velocity profiles for $Re = 180$ reveal the presence of oscillations along the leading face of the cylinder (figure 3). The profiles are shown from the leading edge ($\alpha = 0$) to $\alpha = 125°$, which is beyond the time-averaged separation angle, $\overline{\alpha_s}$. (Note that to preserve the idea of the mean flow moving clockwise along the 'positive' face of the cylinder ($y > 0$), the velocity component $u_\alpha = -u_\theta$ is plotted instead of the natural u_θ.) These oscillations, which have a frequency equal to the wake oscillation frequency, are more evident close to the leading edge, where the flow may reverse in direction. In this figure, the small circles signify the location of the instantaneous velocity maximum, a quantity which exhibits considerable variation close to the leading edge and near the separation angle.

Although there are many theoretical and numerical studies of flow past a circular cylinder with oscillatory boundary conditions (Glauert 1956; Watson 1959; Hori 1962; Childs & Mayle 1984), they do not pertain here, as the strength and extent of the self-induced oscillations vary spatially. A map of the local amplitude of the oscillations of the tangential velocity for $Re = 180$ demonstrates this spatial variability (figure 4).

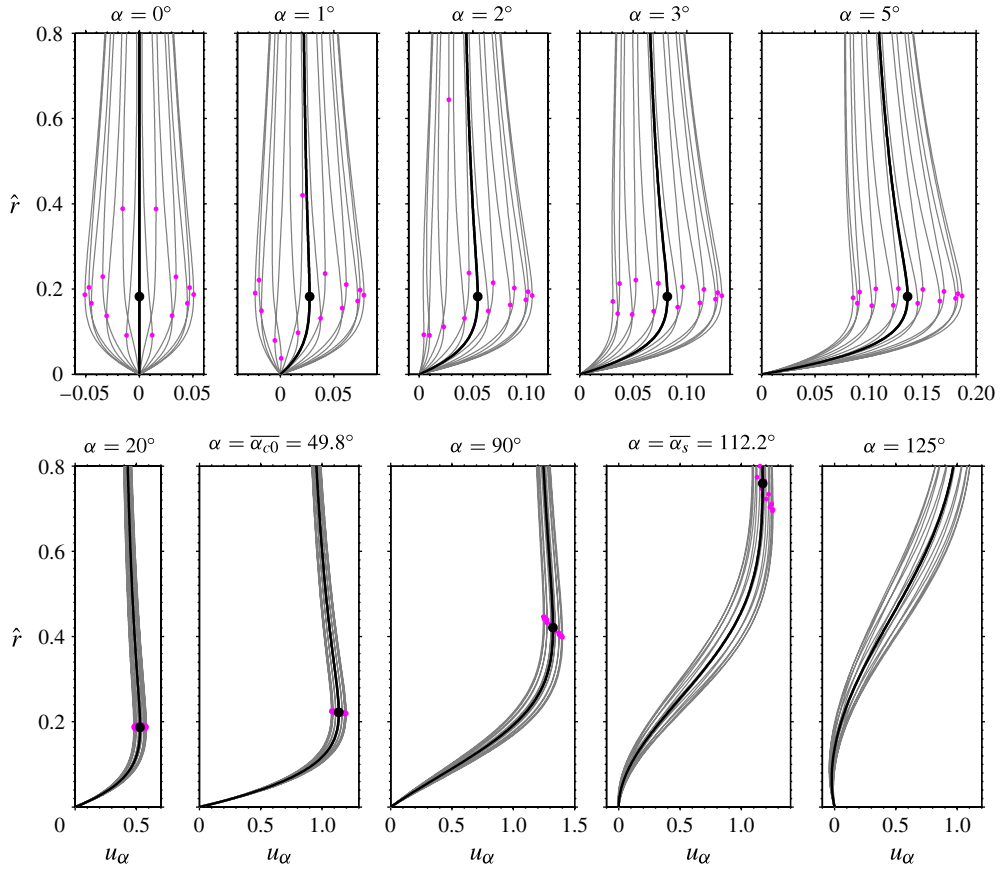

FIGURE 3. (Colour online) Instantaneous (light grey) profiles of tangential velocity in the α direction ($u_\alpha = -u_\theta$) along the collector perimeter for $Re = 180$. Here $\hat{r}$ is the radial coordinate measured from the cylinder surface. The black lines represent the time-averaged profiles, with the black circles showing the edge of the boundary layer (taken as the point of zero velocity gradient). The small circles indicate the point of zero gradient closest to the collector in each instantaneous velocity profile. Note the different scale of the horizontal axis (u_α) for the profiles close to the leading edge ($\alpha \leqslant 5°$). $\overline{\alpha_{c0}}$ is the time average of the maximum angle of capture of particles of vanishing size ($r_p \to 0$) and $\overline{\alpha_s}$ is the time-averaged separation angle.

Here, the amplitude of oscillation is defined as the maximum of the difference between the instantaneous and the time-averaged non-dimensional velocity component:

$$A_{u\theta}(r, \theta) = \max(|u_\theta(r, \theta, t) - \overline{u_\theta}(r, \theta)|). \tag{3.4}$$

It is clear that $A_{u\theta}$ varies with θ and r. Close to the leading face, $A_{u\theta}$ exhibits a local maximum at the edge of the boundary layer; this maximal value increases from approximately 0.05 at $\alpha = 0$ to 0.15 at $\overline{\alpha_s}$ (see also figure 3). Although upstream oscillation amplitudes are small compared with those in the wake, they are far from negligible in the context of particle capture; as will be shown in § 4.4, the upstream oscillations deflect approaching particles around alternating sides of the collector. Finally, the amplitude of oscillation of the tangential velocity depends strongly on *Re*, this dependence varying with the flow regime (figure 5).

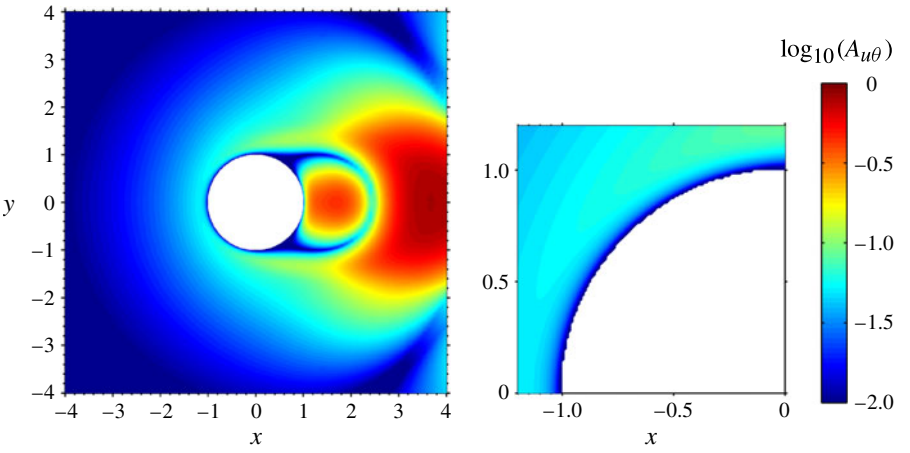

FIGURE 4. The spatial variation of the non-dimensional amplitude of oscillation of the tangential velocity component $A_{u\theta}$ (logarithmic colour scale) for $Re = 180$. Close to the leading face, $A_{u\theta}$ exhibits a local maximum at the edge of the boundary layer which increases from approximately $A_{u\theta} \approx 0.05$ at $\alpha = 0$ to $A_{u\theta} \approx 0.15$ at the separation angle.

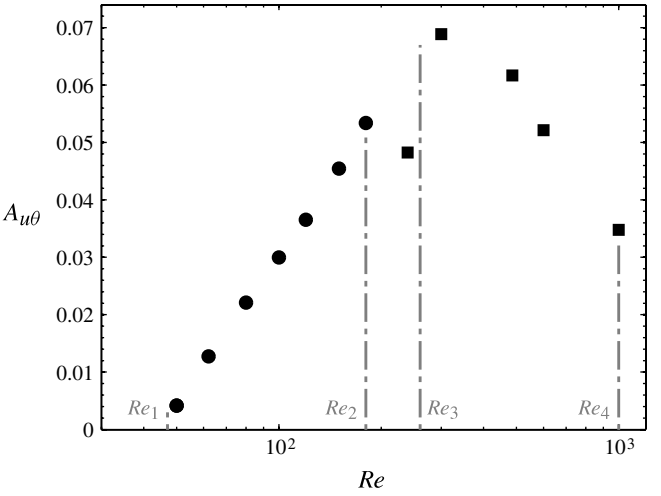

FIGURE 5. The maximum amplitude of oscillation of the tangential velocity at $\alpha = 0$ as a function of Re. (●) Two-dimensional DNS. (■) Three-dimensional DNS. (The vertical lines indicate the regime transitions as explained in §§ 1 and 3.1.)

4. Particle capture

4.1. *Temporal variation*

Previous research into particle capture in steady flow has shown that, for a given particle size, capture efficiency can be estimated by radially integrating the tangential velocity at the maximum angle of capture (Espinosa-Gayosso *et al.* 2012). The maximum angle of capture (θ_c or α_c) is defined by the trajectory of the outermost particle that can be captured: the limiting particle trajectory (see figure 1). As low-inertia particles follow the fluid exactly, the limiting particle trajectory terminates at the point where the radial velocity of the fluid switches from negative (particle moving

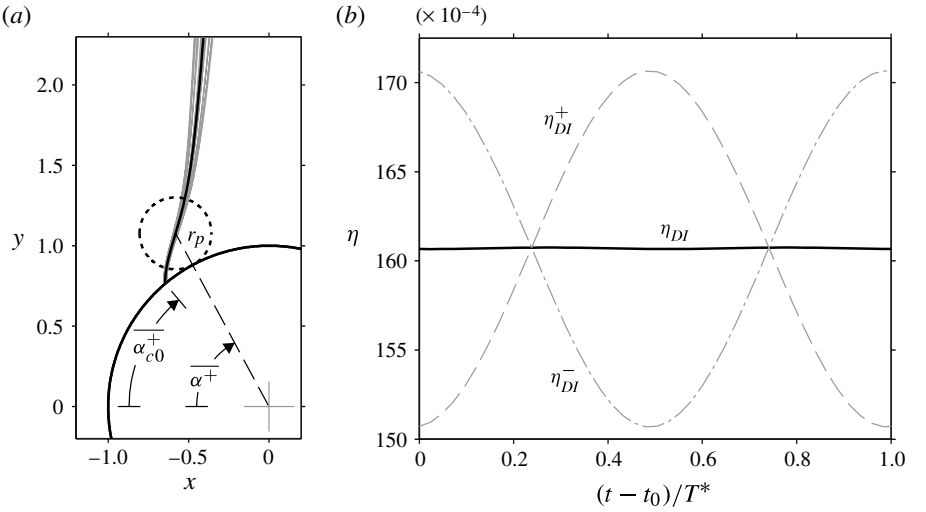

FIGURE 6. Temporal variation of variables related to particle capture for $Re = 180$. (*a*) Instantaneous (light grey) and time-averaged (black) curves of points of zero radial velocity on the 'positive' side of the collector. The time-averaged maximum angle of capture ($\overline{\alpha^+}$) for a particle of given size ratio (r_p) is greater than the time-averaged maximum angle of capture ($\overline{\alpha^+_{c0}}$) for particles of vanishing size ($r_p \to 0$). (*b*) Temporal fluctuation of side ($\eta^{\pm}_{DI}$) and overall (η_{DI}) capture efficiencies for $r_p = 0.01$ during one wake oscillation (of period T^*), starting at an arbitrary instant t_0.

towards the cylinder) to positive (moving away from the cylinder) at a distance equal to the particle radius (where the particle just touches the cylinder surface). For unsteady flow, the maximum angle of capture for given r_p and Re, $\theta_c(t; r_p, Re)$, varies with time but is still determined by the condition of zero radial velocity:

$$u_r(r = 1 + r_p, \theta = \theta_c(t; r_p, Re), t; Re) = 0. \tag{4.1}$$

As can be inferred from (4.1), the collector has two values of θ_c (one on either side of the symmetry plane $y = 0$), both of which oscillate in time. We use the symbol $\theta^+_c(t; r_p, Re)$ (or α^+_c) for the maximum angle of capture on the 'positive' side ($y > 0$) and $\theta^-_c(t; r_p, Re)$ (or α^-_c) for that on the 'negative' side ($y < 0$) of the collector. Figure 6(*a*) shows the instantaneous and time-averaged profiles of points of zero radial velocity for $Re = 180$. When measured clockwise from the leading edge, the maximum angle of capture (α^+_c) increases with r_p. We use the subscript '$c0$' to denote the maximum angle of capture of particles of vanishing size ($r_p \to 0$). (The tangential velocity profile at $\alpha = \overline{\alpha_{c0}} \equiv \overline{\alpha^+_{c0}}$ is shown in figure 3.)

Capture efficiency can thus be defined on either side of the plane of symmetry: η^+_{DI} and η^-_{DI}. These side-efficiency estimates are obtained through radial integration of the tangential velocity at $\theta = \theta^+_c(t; r_p, Re)$ and $\theta^-_c(t; r_p, Re)$:

$$\eta^+_{DI}(t; r_p, Re) = \int_{r=1}^{r=1+r_p} -u_\theta \left(r, \theta^+_c(t; r_p, Re), t; Re\right) \mathrm{d}r \tag{4.2a}$$

$$\eta^-_{DI}(t; r_p, Re) = \int_{r=1}^{r=1+r_p} u_\theta \left(r, \theta^-_c(t; r_p, Re), t; Re\right) \mathrm{d}r. \tag{4.2b}$$

The overall capture efficiency is the average of the two side-efficiencies:

$$\eta_{DI}(t; r_p, Re) = \tfrac{1}{2}\eta_{DI}^{+}(t; r_p, Re) + \tfrac{1}{2}\eta_{DI}^{-}(t; r_p, Re). \tag{4.3}$$

The temporal behaviour of the side and overall capture efficiencies for $Re = 180$ and $r_p = 0.01$ is shown in figure 6(*b*), where $T^* = TU_\infty/R$ is the non-dimensional period of oscillation of the wake. While the unsteady velocity field generates oscillations in the side efficiencies, these oscillations are out of phase such that the overall capture efficiency remains effectively constant.

4.2. *Time-averaged capture efficiency*

As the time-averaged flow is symmetric with respect to the $y = 0$ plane, the time-averaged capture efficiencies are identical:

$$\overline{\eta_{DI}} = \overline{\eta_{DI}^{+}} = \overline{\eta_{DI}^{-}}. \tag{4.4}$$

Furthermore, the difference between $\overline{\eta_{DI}}$ and the capture efficiency estimated from the time-averaged velocity field ($\widetilde{\eta_{DI}}$) was found to be negligible for all Re and r_p analysed here. That is,

$$\overline{\eta_{DI}}(r_p, Re) \approx \widetilde{\eta_{DI}}(r_p, Re) = \int_{r=1}^{r=1+r_p} -\overline{u_\theta}(r, \overline{\theta_c}(r_p, Re); Re)\,\mathrm{d}r, \tag{4.5}$$

where

$$\overline{\theta_c} = \overline{\theta_c^{+}} = -\overline{\theta_c^{-}} \tag{4.6}$$

is defined by the time-averaged curve of zero radial velocity (figure 6*a*).

We have applied (4.5) to the numerically generated two- and three-dimensional flow fields to estimate time-averaged capture efficiencies due to direct interception in the range $47 < Re \leqslant 1000$. This methodology assumes that forces on the particles such as lift induced by shear, van der Waals attraction and hydrodynamic repulsion to contact may be neglected to leading order, and we test this by comparing our particle-capture estimates against existing experimental data. Our estimates are in excellent agreement with the experiments of Palmer *et al.* (2004) and lie within their experimental range of error (figure 7). Note that results for $Re < 47$ are taken from Espinosa-Gayosso *et al.* (2012).

4.3. *The dependence of capture efficiency on Re and r_p*

As discussed in § 1, existing analytical expressions for particle capture do not fully demonstrate the dependence of capture efficiency on Re and r_p. The quadratic dependence on r_p is obtained through the approximation of a linear time-averaged profile of tangential velocity ($u_\theta(r)$) in (4.5). That is,

$$\overline{\eta_{DI}}(r_p, Re) \approx \int_{r=1}^{r=1+r_p} |\overline{g_{c0}}(Re)|(r-1)\,\mathrm{d}r = \frac{1}{2}|\overline{g_{c0}}(Re)|{r_p}^2, \tag{4.7}$$

where

$$\overline{g_{c0}}(Re) \equiv \left.\frac{\partial \overline{u_\theta}(r, \overline{\theta_{c0}}; Re)}{\partial r}\right|_{r=1} \tag{4.8}$$

is the time-averaged gradient of tangential velocity at the collector surface evaluated at the maximum angle of capture for particles of vanishing size. However, this approximation of a linear velocity profile (4.7) is only valid in the limit of very

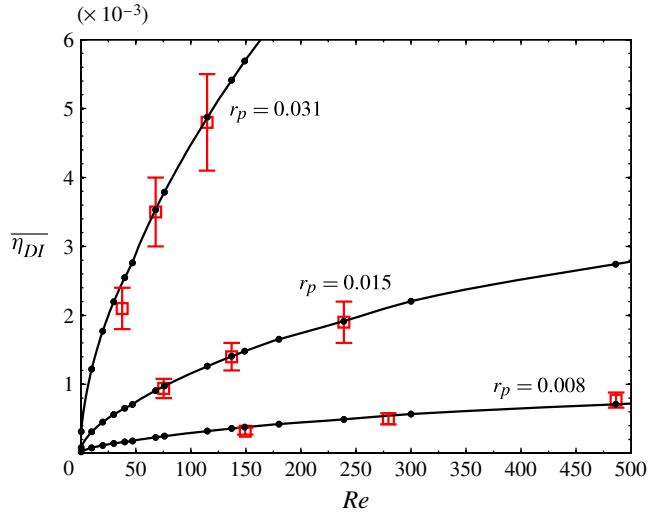

FIGURE 7. (Colour online) The agreement of DNS estimates (●) of time-averaged capture efficiency by direct interception ($\overline{\eta_{DI}}$) with experimental data from Palmer *et al.* (2004) (□), where the error bars represent the standard error. Dots are placed at the Reynolds numbers at which DNS were performed and the solid lines represent interpolated capture efficiency curves for each particle size ratio (r_p). Results for $Re < 47$ were obtained from Espinosa-Gayosso *et al.* (2012).

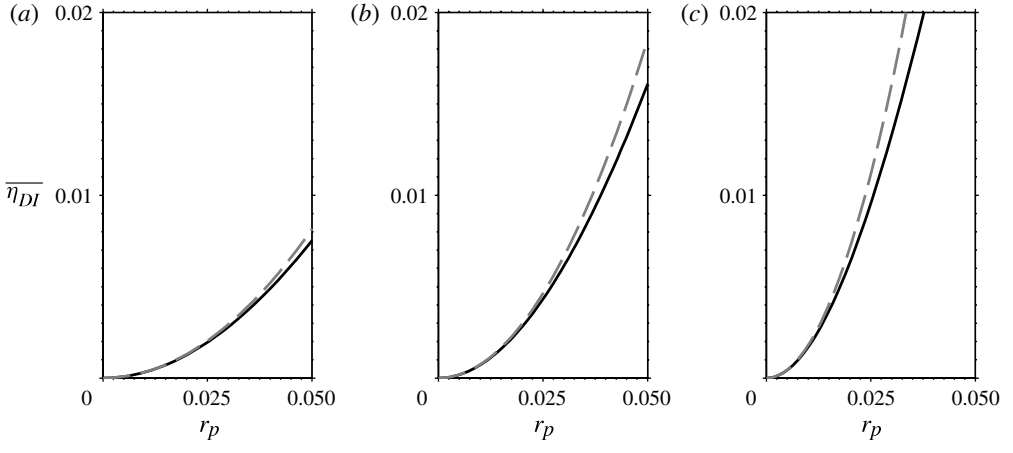

FIGURE 8. The quadratic dependence of capture efficiency on r_p applies only to small particle size ratios, as shown by the comparison of approximation (4.7) (−−) with estimates from DNS (—): (*a*) $Re = 50$; (*b*) $Re = 180$; and (*c*) $Re = 1000$.

low particle size, as can be seen in the velocity profile at $\alpha = \overline{\alpha_{c0}}$ (figure 3). This is further demonstrated in figure 8, where estimates of particle capture efficiency using (4.7) are compared with those obtained from DNS.

The dependence of capture efficiency on *Re* will first be analysed for particles of vanishing size. It is important to note that the capture efficiency of small particles is directly proportional to the surface velocity gradient $\overline{g_{c0}}$ (Weber & Paddock

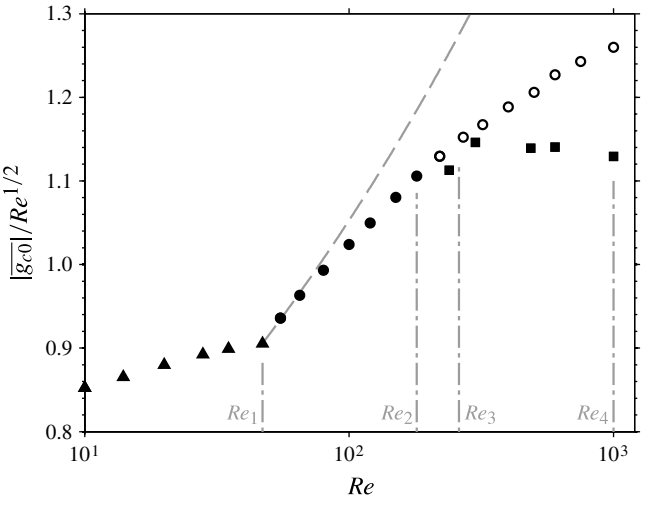

FIGURE 9. The dependence on Re of the time-averaged maximum velocity gradient at the collector surface ($|\overline{g_{c0}}|$, to which the capture efficiency of small particles is directly proportional). DNS results (two-dimensional steady flow DNS (Espinosa-Gayosso *et al.* 2012) (▲), present two-dimensional DNS ($Re \leqslant Re_2 \simeq 180$) (●) and present three-dimensional DNS (■)) show the changes in behaviour across the different flow regimes. Hypothetical results from two-dimensional DNS above $Re = Re_2$ are also shown (○). The dashed line (−−) represents a $|\overline{g_{c0}}| \sim Re^{0.7}$ relationship. (The vertical lines indicate the regime transitions, as explained in §§ 1 and 3.1.).

1983; Espinosa-Gayosso *et al.* 2012), as can be inferred from (4.7). (Also, $\overline{g_{c0}}$ is the maximum value of the surface velocity gradient, and $\overline{\theta_{c0}}$ can therefore be interpreted as the angle of maximum local skin friction or maximum vorticity at the cylinder surface.) Figure 9 shows the complex behaviour of the scaled velocity gradient $|\overline{g_{c0}}|/Re^{1/2}$ with Re. Immediately after the onset of vortex shedding (at Re_1), $|\overline{g_{c0}}|$ increases significantly, together with an increase in the base suction (see also figure 2*a*). Close to this point, the dependence $|\overline{g_{c0}}| \sim Re^{0.7}$ suggested by existing studies (as explained in § 1 and indicated here by a dashed curve) seems to apply but is valid only for $47 < Re \lesssim 100$, and its usage for higher Re may induce large errors. Across the full range of two-dimensional vortex shedding ($Re_1 < Re < Re_2$), the maximum velocity gradient is better described by $|\overline{g_{c0}}| \sim Re^{0.65}$. The behaviour of the scaled gradient changes as the flow transits into the regimes of three-dimensional vortex shedding. In the range ($Re_3 < Re \lesssim 1000$), the theoretical high-Re dependence $|\overline{g_{c0}}| \sim Re^{1/2}$ (Schlichting 1979) is practically established, although this dependence is expected to change again after the flow transition at $Re_4 \simeq 1000$.

The error associated with estimation of capture efficiency of small particles from two-dimensional DNS beyond $Re = Re_2 \simeq 180$ can also be observed in figure 9. Relative to three-dimensional DNS, hypothetical two-dimensional estimates (shown as unfilled circles) overestimate the velocity gradient (and, therefore, the capture efficiency); this overestimate reaches 13 % at $Re = 1000$. Estimates from the hypothetical two-dimensional DNS also fail to approach the theoretical high-Re dependence, $\overline{\eta_{DI}} \sim Re^{1/2}$. This failure is not due to the direct effect of oscillations on particle trajectories, as hypothesized by Haugen & Kragset (2010), but arises when performing two-dimensional simulations of a highly three-dimensional flow.

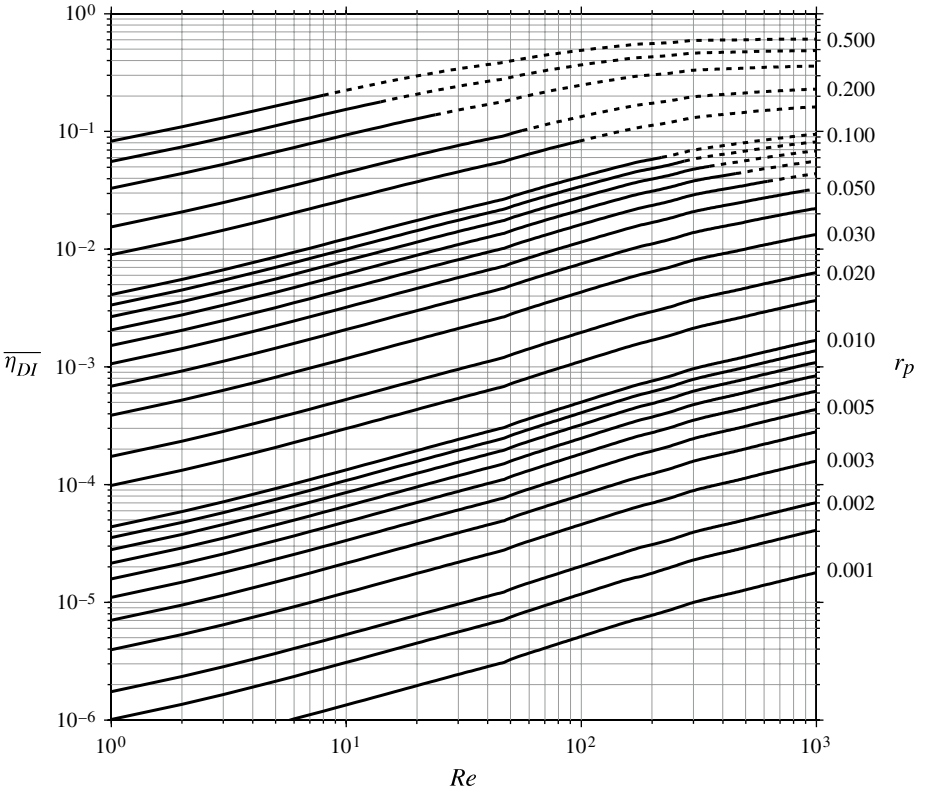

FIGURE 10. Mean capture efficiency by direct interception ($\overline{\eta_{DI}}$) of a circular cylinder. Here Re is the Reynolds number based on the diameter of the collector and r_p is the particle–collector radius ratio. Each line corresponds to a particular value of r_p (labelled on the right). Dotted lines represent the region where the Stokes number exceeds 0.25 (for neutrally buoyant particles), such that particle inertia may influence particle capture.

To summarize the results, the dependence of the capture efficiency on Re and r_p is presented in figure 10 for the range $1 \leqslant Re \leqslant 1000$ and $0.001 \leqslant r_p \leqslant 0.5$ (results for $Re < 47$ are taken from Espinosa-Gayosso *et al.* (2012)). For small particles, the capture efficiency by direct interception behaves as explained in the preceding paragraphs of this section. For large particles, the capture efficiency becomes independent of Reynolds number at large Re; more precisely, this occurs once the particle size significantly exceeds the boundary layer thickness. The dotted lines represent the region where, for neutrally buoyant particles, the Stokes number exceeds 0.25, the critical value (for $Re \leqslant 1000$) above which particle inertia becomes important (Phillips & Kaye 1999). Inertial impaction may not be negligible in this region. This diagram can be used for direct estimates of particle capture efficiency for given Re and r_p. (For the corresponding diagram at lower Re, see Espinosa-Gayosso *et al.* (2012).)

4.4. *Effects of oscillations on particle trajectories*

When vortex shedding is present, the self-induced oscillations upstream of the cylinder (see § 3.2) affect particle trajectories, modifying the simple steady flow conceptualization illustrated in figure 1. Particle trajectories, calculated from the DNS-

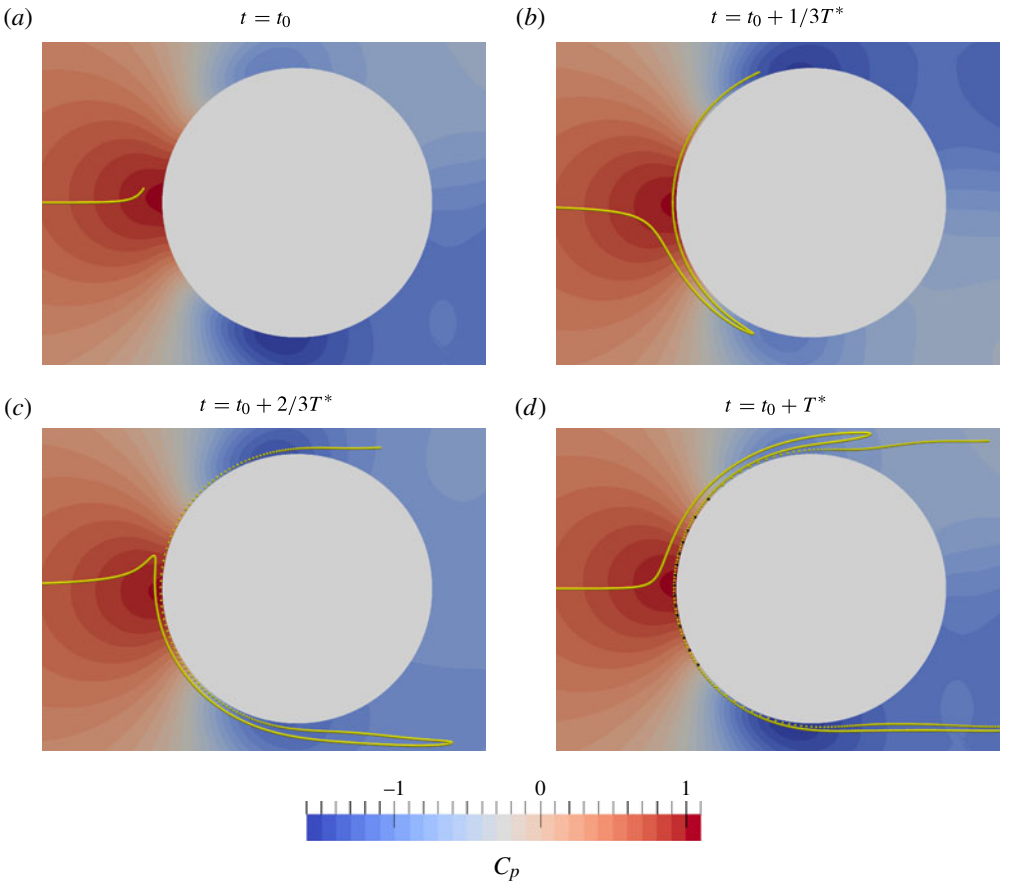

FIGURE 11. Oscillations, induced by vortex shedding, near the leading face of the collector stretch and bend a line of particles (shown in yellow) towards alternating sides of the cylinder. The line of particles ($r_p = 0.01$) was initially released upstream of the cylinder at the symmetry plane ($y = 0$). The figures show snapshots at: (*a*) $t = t_0$, where t_0 is an arbitrary instant; (*b*) $t = t_0 + 1/3T^*$; (*c*) $t = t_0 + 2/3T^*$; and (*d*) $t = t_0 + T^*$, where T^* is the period of wake oscillation. Whereas in the case of steady upstream flow, all released particles would be captured, only a small fraction of particles (shown in black) are captured here, highlighting the importance of upstream oscillations in the particle-capture process. The background colour indicates the instantaneous pressure coefficient $C_p = 2(p - p_\infty)$. The Reynolds number is 180.

generated flow field, demonstrate this modification. Trajectories were obtained with a second-order temporal scheme, using the same time step as in the DNS. A linear piecewise spatial interpolation scheme (which generates a continuous velocity field at any position in the domain) was used for estimating particle velocity, which was taken as that of the fluid at the position of the particle centre.

The influence of upstream oscillations on particle trajectories is best illustrated by the deformation of a line of particles released along the symmetry plane (figure 11). The line of 10 000 particles ($r_p = 0.01$) was released far upstream of the collector (in the range $-160 \leqslant x \leqslant -140$) with equal spacing between particle centres. As we do

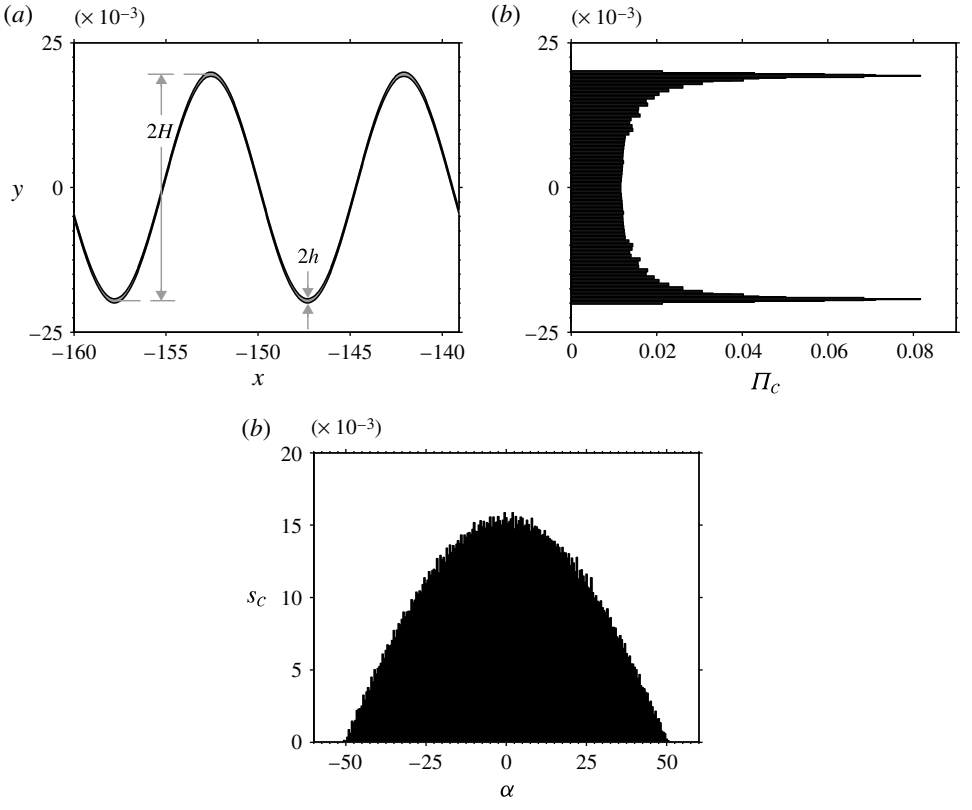

FIGURE 12. Analysis of the spatial variation of particle capture for $r_p = 0.01$ and $Re = 180$. (*a*) The upstream *y*-coordinates of particles that were captured on the leading face. The upstream oscillations clearly modify the steady flow conceptualization of particle capture: while the upstream positions still lie within a thin strip of width $2h$, the strip has a near-sinusoidal deformation of amplitude H. (*b*) The probability of capture (Π_c) for a given particle as a function of upstream position. Capture probability is greatest at the edges of the upstream window of capture and lowest at $y = 0$; at all positions, $\Pi_c \ll 1$. (*c*) The probability density function $s_c(\alpha)$ of the location of captured particles on the collector surface. s_c has a maximum at the leading edge of the collector ($\alpha = 0$). For particles of vanishing size, the maximum angle of capture is consistently $\pm 50°$ in the vortex-shedding regime.

not consider interaction between particles, they were allowed to overlap in space to form an unbroken line (shown in yellow). Importantly, in the case of steady upstream flow, all particles in the line would be captured; that this does not happen here highlights the influence of flow unsteadiness. As the particles approach the collector, the tip of the particle line is deflected (figure 11*a*). (This first snapshot is for an arbitrary instant $t = t_0$.) As time progresses, the line of particles is then bent around the negative side of the collector, while a segment following the tip continues to be stretched towards the positive side; this generates a 'belt' of particles around the leading face of the collector (figure 11*b*). When the flow close to the leading edge reverses direction (figure 11*c*), the line is again stretched towards the positive side. The stretching near the leading face is now more evident, as individual particles (none of which have yet made contact with the collector) can be distinguished. After the full cycle is completed (figure 11*d*), a second belt is formed. Only a small fraction

of particles from the first belt are captured (shown in black). This suggests that in contrast to steady upstream flow (where particles in a narrow upstream window are all captured), the upstream window of capture is much broader in the vortex-shedding regime.

To identify the upstream window of capture (again for the case of $Re = 180$ and $r_p = 0.01$), a cloud of particles was released in the area ($-160 \leqslant x \leqslant -140$, $-1 \leqslant y \leqslant 1$). The initial position of particles captured on the leading face of the collector is shown in figure 12(*a*) (the fraction of particles captured on the lee side of the collector was less than 5 %, and their initial positions are not shown). The initial lateral positions of captured particles still lie within a thin strip whose width is related to capture efficiency by (1.7), such that $2h = \overline{\eta_{DI}}D$ remains applicable. However, due to the near-sinusoidal shape of this strip, captured particles now come from a much wider upstream window of capture (of width $2(H + h)$, where H is the amplitude of the strip's sinusoidal shape). The probability of capture for a given particle $\Pi_c(y)$ depends on its initial y coordinate (figure 12*b*). Particles initially at the symmetry plane are the least likely to be captured within the upstream window of capture ($\Pi_c(y = 0) = 0.011$), with maximal capture probability at the edges of the window of capture. To summarize, in the case of steady upstream flow, all particles released within $\pm h$ of the symmetry plane are captured. In the vortex-shedding regime, a small fraction of particles released within the much wider $\pm(H + h)$ range are captured, with capture probability varying with upstream position.

The probability density function (s_c) of the location of captured particles on the collector surface is shown in figure 12(*c*). Capture is most likely to occur at the leading edge ($\alpha = 0$), with the probability decaying to zero at the maximum angle of capture. For the range of Re analysed ($47 < Re \leqslant 1000$), the maximum angle of capture for particles of vanishing size remained virtually constant $\overline{\alpha_{c0}} \approx 50°$. This is in good agreement with the experiments of Palmer *et al.* (2004) and with our previous low-Re steady-state particle capture analysis (Espinosa-Gayosso *et al.* 2012).

5. Conclusions

We have used two- and three-dimensional DNS to obtain estimates of the capture efficiency of low-inertia particles by cylindrical collectors in ranges relevant to aquatic systems: $47 < Re \leqslant 1000$ and $0 < r_p \leqslant 0.5$. Our analysis allows us to present, for the first time, a physically based description of capture efficiency by direct interception in the vortex-shedding regime. The accuracy of the results is confirmed by their excellent agreement with experiment.

The transition of flow around a circular cylinder set by changing Re induces shifts in behaviour of commonly employed flow descriptors (namely the drag coefficient, the base suction coefficient and the Strouhal number). Such changes are also observed in the capture efficiency. In the range $260 \lesssim Re \lesssim 1000$, where vortex shedding is three-dimensional, the capture efficiency of small particles is well-approximated by $\eta_{DI} \sim Re^{1/2}$, the dependence predicted by high-Re boundary-layer theory. For particle sizes with radius significantly exceeding the boundary-layer thickness, capture efficiency by direct interception becomes independent of the Reynolds number as it increases.

Vortex shedding induces oscillations upstream of the cylinder which considerably influence the trajectories of low-inertia particles. These oscillations cause the particle capture process in the vortex-shedding regime to be significantly different from the case of steady upstream flow. Most notably, in the vortex-shedding regime: (i) the

upstream window of capture is much wider; (ii) the probability of capture for particles in the window is $\ll 1$; and (iii) particles along the symmetry plane ($y = 0$) are not the most likely to be captured.

Acknowledgements

A.E.-G. acknowledges the scholarships granted by CONACyT-Banco de México, the Australian Government (IPRS) and The University of Western Australia. The authors are grateful to the iVEC supercomputing facility for the resources granted to this study. This research was supported by an Australian Research Council Discovery Project (DP35603400).

REFERENCES

ACKERMAN, J. D. 2006 Sexual reproduction of seagrasses: pollination in the marine context. In *Seagrasses: Biology, Ecology and Conservation* (ed. A. W. D. Larkum, R. J. Orth & C. M. Duarte), Springer.

BLOOR, M. S. 1964 The transition to turbulence in the wake of a circular cylinder. *J. Fluid Mech.* **19** (2), 290–304.

BOUHAIRIE, S. & CHU, V. H. 2007 Two-dimensional simulation of unsteady heat transfer from a circular cylinder in crossflow. *J. Fluid Mech.* **570**, 177–215.

BRAZA, M., CHASSAING, P. & MINH, H. H. 1986 Numerical study and physical analysis of the pressure and velocity fields in the near wake of a circular cylinder. *J. Fluid Mech.* **165**, 79–130.

CHILDS, E. P. & MAYLE, R. E. 1984 Heat transfer on a rotationally oscillating cylinder in cross-flow. *Intl J. Heat Mass Transfer* **27** (1), 85–94.

DWYER, H. A. & MCCROSKEY, W. J. 1973 Oscillating flow over a cylinder at large Reynolds-number. *J. Fluid Mech.* **61** (4), 753–767.

ESPINOSA-GAYOSSO, A., GHISALBERTI, M., IVEY, G. N. & JONES, N. L. 2012 Particle capture and low-Reynolds-number flow around a circular cylinder. *J. Fluid Mech.* **710**, 362–378.

FERZIGER, J. H. & PERIC, M. 2002 *Computational Methods for Fluid Dynamics*, 3rd edn. Springer.

FRIEDLANDER, S. K. 2000 *Smoke, Dust and Haze. Fundamentals of Aerosol Dynamics*, 2nd edn. Oxford University Press.

GLAUERT, M. B. 1956 The laminar boundary layer on oscillating plates and cylinders. *J. Fluid Mech.* **1** (1), 97–110.

HARVEY, M., BOURGET, E. & INGRAM, R. G. 1995 Experimental evidence of passive accumulation of marine bivalve larvae on filamentous epibenthic structures. *Limnol. Oceanogr.* **40** (1), 94–104.

HAUGEN, N. E. L. & KRAGSET, S. 2010 Particle impaction on a cylinder in a crossflow as function of Stokes and Reynolds numbers. *J. Fluid Mech.* **661**, 239–261.

HENDERSON, R. D. 1995 Details of the drag curve near the onset of vortex shedding. *Phys. Fluids* **7** (9), 2102–2104.

HENDERSON, R. D. 1997 Nonlinear dynamics and pattern formation in turbulent wake transition. *J. Fluid Mech.* **352**, 65–112.

HORI, E.-I. 1962 Unsteady boundary layers, 3rd report, boundary layer on a circular cylinder in rotational oscillation. *Bull. JSME* **5** (17), 64–72.

ISSA, R. I. 1986 Solution of the implicitly discretized fluid-flow equations by operator-splitting. *J. Comput. Phys.* **62** (1), 40–65.

JORDAN, S. K. & FROMM, J. E. 1972 Oscillatory drag, lift, and torque on a circular cylinder in a uniform flow. *Phys. Fluids* **15** (3), 371–376.

LANGE, C. F., DURST, F. & BREUER, M. 1998 Momentum and heat transfer from cylinders in laminar crossflow at $10^{-4} \leqslant Re \leqslant 200$. *Intl J. Heat Mass Transfer* **41** (22), 3409–3430.

NORBERG, C. 1994 An experimental investigation of the flow around a circular cylinder: influence of aspect ratio. *J. Fluid Mech.* **258**, 287–316.

PALMER, M. R., NEPF, H. M., PETTERSSON, T. J. R. & ACKERMAN, J. D. 2004 Observations of particle capture on a cylindrical collector: implications for particle accumulation and removal in aquatic systems. *Limnol. Oceanogr.* **49** (1), 76–85.

PARNAS, R. & FRIEDLANDER, S. K. 1984 Particle deposition by diffusion and interception from boundary-layer flows. *Aerosol Sci. Technol.* **3** (1), 3–8.

PAXSON, D. E. & MAYLE, R. E. 1990 Velocity measurements on the forward portion of a cylinder. *Trans. ASME J. Fluids Engng* **112** (2), 243–245.

PHILLIPS, C. G. & KAYE, S. R. 1999 The influence of the viscous boundary layer on the critical Stokes number for particle impaction near a stagnation point. *J. Aerosol. Sci.* **30** (6), 709–718.

POSDZIECH, O. & GRUNDMANN, R. 2001 Numerical simulation of the flow around an infinitely long circular cylinder in the transition regime. *Theor. Comput. Fluid Dyn.* **15** (2), 121–141.

POSDZIECH, O. & GRUNDMANN, R. 2007 A systematic approach to the numerical calculation of fundamental quantities of the two-dimensional flow over a circular cylinder. *J. Fluids Struct.* **23** (3), 479–499.

SCHLICHTING, H. 1979 *Boundary-layer Theory*, 7th edn. McGraw-Hill.

SHIMETA, J. & KOEHL, M. A. R. 1997 Mechanisms of particle selection by tentaculate suspension feeders during encounter, retention, and handling. *J. Expl Mar. Biol. Ecol.* **209** (1–2), 47–73.

WATSON, J. 1959 The two-dimensional liminar flow near the stagnation point of a cylinder which has an arbitrary transverse motion. *Q. J. Mech. Appl. Maths* **12** (2), 175–190.

WEBER, M. E. & PADDOCK, D. 1983 Interceptional and gravitational collision efficiencies for single collectors at intermediate Reynolds-numbers. *J. Colloid Interface Sci.* **94** (2), 328–335.

WIESELSBERGER, C. 1921 Neuere feststellungen über die gesetze des flüssigkeits- und luftwiderstands. *Phys. Z.* **22**, 321–328.

WILDISH, D. & KRISTMANSON, D. 1997 *Benthic Suspension Feeders and Flow*, 1st edn. Cambridge University Press.

WILLIAMSON, C. H. K. 1988 The existence of two stages in the transition to three-dimensionality of a cylinder wake. *Phys. Fluids* **31** (11), 3165–3168.

WILLIAMSON, C. H. K. 1996 Vortex dynamics in the cylinder wake. *Annu. Rev. Fluid Mech.* **28**, 477–539.

WILLIAMSON, C. H. K. & ROSHKO, A. 1990 Measurements of base pressure in the wake of a cylinder at low Reynolds numbers. *Z. Fluwiss. Weltraumforsch.* **14** (1–2), 38–46.

WU, M. H., WEN, C. Y., YEN, R. H., WENG, M. C. & WANG, A. B. 2004 Experimental and numerical study of the separation angle for flow around a circular cylinder at low Reynolds number. *J. Fluid Mech.* **515**, 233–260.

ZDRAVKOVICH, M. M. 1997 *Flow Around Circular Cylinders. Vol. 1: Fundamentals*. Oxford University Press.